IIETA International Information and Engineering Technology Association
Advancing the World of Information and Engineering

Journal Européen des Systèmes Automatisés
Vol. 57, No. 5, October, 2024, pp. 1305-1320
Journal homepage: http://iieta.org/journals/jesa

Enhancing Grid Stability and Efficiency: Cost-Effective Hardware Implementation for Advanced Control of Grid-Connected PV Systems

Amal Satif[1*], Laamari Hlou[2], Mohcin Mekhfioui[3], Rachid Elgouri[1]

[1] Laboratory of Advanced Systems, ENSA, Kenitra 14000, Morocco
[2] Laboratory of Electrical Engineering & Energy Systems, Ibn Tofail University, Kenitra 14000, Morocco
[3] Green Tech Institute (GTI), Mohammed VI Polytechnic University, Benguerir 43150, Morocco

Corresponding Author Email: amal.satif@uit.ac.ma

https://doi.org/10.18280/jesa.570506

Received: 17 July 2024
Revised: 29 September 2024
Accepted: 10 October 2024
Available online: 28 October 2024

Keywords:
photovoltaic systems, inverter, synchronization, SVPWM, cost-effective implementation, experimental results

ABSTRACT

Grid-connected systems are increasingly becoming essential complements to existing electricity infrastructures in many developed countries. Among renewable energy systems, photovoltaic (PV) panels are the most utilized and efficient. However, integrating PV systems into the main grid presents substantial challenges. To overcome these issues, this paper presents a comprehensive approach through the design, control, and hardware implementation of a cost-effective grid-connected PV (GPV) system. Focusing on practical and economical solutions, this research transcends theoretical simulations by developing a tangible laboratory-scale prototype. This prototype integrates both power and control subsystems to ensure efficient and reliable operation of GPV systems. The power subsystem comprises a three-phase inverter, an LCL filter, and an interface circuit, forming the core hardware for energy conversion and grid connection. The control subsystem incorporates enhanced and advanced control techniques to optimize performance. These include the DSOGI-PLL synchronization algorithm, which guarantees precise grid voltage phase angle detection even when noise and higher-order harmonics are present, facilitating seamless grid integration. Additionally, the Space Vector Pulse Width Modulation (SVPWM) algorithm is employed to control the three-phase voltage source inverter, providing superior DC-link voltage utilization and harmonic performance. A robust current PI controller is also implemented, offering excellent steady-state response and resilience against system parameter variations. The results obtained have proven that the connection of the proposed system can be successfully achieved and implemented. This work promotes the widespread adoption of photovoltaic systems and contributes to global sustainable energy initiatives.

1. INTRODUCTION

Electricity has become a vital product for humanity. It is produced by large power plants that transform primary energy into electrical energy, which is then transported and distributed to consumers. Like fire in prehistoric times, electricity has changed human life. The vital impact of electricity on our daily lives is particularly noticeable during power supply interruptions [1]. Moreover, uncontrolled power outages can lead to significant societal and economic threats. There are notable examples of outages that have occurred in recent years around the world and their impacts in terms of the number of people affected: in September 2003, a power outage affected all of Italy (except two of its islands) for twelve hours; in the same year, the power outage in the northeastern United States and southeastern Canada left forty million people in the dark; in September 2005, the outage in Java-Bali, Indonesia, affected over one hundred million people; while in November 2009, the power outage in Brazil and Paraguay affected about ninety million people.

For these reasons, over the past few decades, the demand for economical, clean, and renewable energy has increased considerably and become a crucial necessity for sustainable development [2]. According to the International Energy Agency (IEA), global renewable energy capacity reached 3,064 gigawatts (GW) in 2021, with an annual increase of 9% from the previous year, highlighting the growing commitment to renewable sources [3]. This surge in renewable energy adoption is partly due to the depletion of industrial fuels, which has prompted a shift towards sustainable alternatives. Additionally, the urgency to reduce greenhouse gas emissions has become more critical; the Global Carbon Project reported that carbon dioxide emissions from fossil fuels rose to 36.4 billion metric tons in 2021 [4], emphasizing the need for cleaner energy sources [5].

1.1 Paper motivation

Among the various renewable energy sources (RES) available, solar energy stands out as a major contender due to its abundance and pollution-free conversion into electricity [6], and its relatively decreasing cost [7]. According to the

International Renewable Energy Agency (IRENA), the global average cost of utility-scale solar photovoltaics (PV) fell by 89% between 2010 and 2021, making it one of the most competitive energy sources [8]. In recent years, the demand for solar energy sources has increased steadily due to several factors, namely the growing efficiency of solar cells and improvements in manufacturing technology. In 2021, the total installed solar capacity worldwide reached 1,000 GW, with a record 168 GW of new capacity added that year alone, highlighting the ongoing trend of connecting PV modules to the distribution grid in many countries [9]. This trend is expected to continue, with projections indicating that global solar capacity could exceed 5,000 GW by 2030. For example, Morocco has proposed action plans in which it is committed to taking full advantage of its triple strategy to adapt to climate change. The main axis of its strategy is that by 2030, the country should cover 50% of its electricity needs from RES [10]. This is a sign of the importance of implementing renewable energies.

PV solar systems are generally used in two main areas:

• Off-grid PV systems: in these systems, distant loads without grid connectivity are powered by solar panels.

• Grid-connected PV systems: with these systems, energy from solar panels is used to power both the electrical grid and nearby loads. This system can be put in parking lot shade structures, building facades, and rooftops, etc. [11].

Given the various GPV projects recently installed in different countries around the world, we can see that GPV systems currently dominate the PV market, particularly in the United States, Europe, and Japan. Despite the importance of this field, GPV systems have not been widely developed in due to technical, economic, and regulatory obstacles, namely:

• Maximum Power Point Tracking (MPPT): Maximizing the power output of PV modules requires efficient MPPT algorithms and technologies, which can be challenging to implement effectively [12-14].

• Voltage Dip Sensitivity: PV systems may be sensitive to voltage dips or fluctuations in the grid [15], which can affect their performance and reliability [16].

• Grid Synchronization: Ensuring that PV systems synchronize properly with the electrical grid is essential for safe and efficient operation. This requires advanced control and monitoring systems [17, 18].

• Cost and Component Density: The cost of PV components, such as inverters, batteries, and mounting structures, can impact the overall affordability and feasibility of PV installations. Additionally, the density of these components may pose challenges in terms of space requirements and installation logistics [19].

It is important to recognize that the increasing interest in PV systems necessitates expanded research and development in areas such as MPPT, grid synchronization, power quality, electronic interfaces, and control mechanisms.

Motivated by the significant demand for PV solar energy and the immediate need to improve GPV systems, the research presented in this paper focuses on the study, design, control, and implementation of a PV energy conversion system, operating at around 1.5 kW of nominal power.

1.2 Paper contribution

The integration of renewable energy sources (RES) into the electrical grid has seen significant growth, driven by global efforts to reduce dependency on fossil fuels and lower greenhouse gas emissions. However, many of these advancements remain at the simulation stage, with limited real-world implementation. For instance, Gao et al. [20] developed a simulation model to address common-mode leakage currents in non-isolated PV grid-connected inverters, using an improved double-vector model predictive current control (IDV-MPCC). While the model successfully demonstrated the suppression of common-mode voltage (CMV) and reduced harmonic distortion, its validation remains theoretical, without physical experimentation.

In another example, Rehan [21] utilized HOMER software to simulate a hybrid renewable energy system incorporating PV, biomass, and hydropower for grid-connected applications. Despite showing promising results in terms of economic feasibility and carbon emission reduction, the study is purely simulation-based and lacks real-world testing. Similarly, Dunna et al. [22] conducted a simulation using the HOMER Pro software to design a hybrid PV/Diesel/Generator system for Douala, Cameroon. The analysis suggested cost savings and improved system reliability, but challenges such as temperature variability and regulatory hurdles highlight the need for practical implementation to fully validate these findings

Most of these research efforts are heavily reliant on simulations using tools like MATLAB/Simulink [23, 24], which facilitate implementation in devices such as dSPACE (Digital Signal Processing and Control Engineering) [25], DSP (Digital Signal Processing) [26, 27], and FPGA (Field-Programmable Gate Array) [28, 29] much easier. However, these platforms are often costly, complex, and bulky, with some requiring a dedicated computer for the execution of control algorithms. This contributes to the high cost and logistical challenges of implementing grid-connected PV (GPV) systems, making them less accessible for widespread deployment.

The aim of this research is to develop a complete laboratory-scale test prototype of a low-power PV system connected to the low-voltage distribution grid, aiming to overcome the challenges mentioned above. This system could be beneficial for future researchers in the field of renewable energies to validate their research work. The proposed energy conversion system offers a promising and cost-effective approach, yielding significant and efficient results for use in GPV projects.

It is worth mentioning that designing and implementing a power system necessitates expertise in multiple areas of electrical and computer engineering. This includes systems theory, circuit analysis, board programming, power electronics, and software development, and feedback control systems.

1.3 Paper outline

This work is structured as follows: In Section 2, Several research studies were examined to uncover innovative contributions in the field. Section 3 outlines the theoretical concepts that must be taken into account and describes the methodology that facilitated the successful implementation of the GPV system. Section 4 is dedicated to the complete implementation of the grid-connected three-phase inverter, including the various control algorithms and components used. The experimental results are detailed in Section 5. Lastly, Section 6 provides the paper's conclusion and discusses future research directions.

2. RELATED WORK

Numerous studies have delved into control strategies and inverter designs within the domain of GPV systems. For instance, a novel control strategy for quasi-Z-source inverters in GPV systems has been proposed to efficiently extract power utilizing MPPT and proportional integral (PI) control, maintaining a unity power factor [30]. It's important to note that this strategy's validation primarily relies on simulation studies using MATLAB/Simulink.

Another significant research avenue focuses on the integrating battery energy storage with PV systems to bolster grid stability and diminish reliance on conventional energy sources [31]. While simulations often form the basis of such investigations, practical implementations are relatively scarce.

In the realm of inverter design, simplified SVPWM techniques have been devised for three-phase inverters, aiming at real-time implementation and showcasing effectiveness in driving inverters [32]. However, these demonstrations typically occur within simulation environments, highlighting a gap in practical validation.

Furthermore, studies have addressed the development of intelligent control algorithms, such as fuzzy-PI controllers, exhibiting promise in enhancing system stability and performance, the prototype proposed in this research demonstrates that the Simulink model can be directly transformed into a control device, validating the proper operation of the fuzzy-PI controller, the design method allows for the controller to be developed without complex programming, using MATLAB Coder to convert the Simulink controller into C code for microcontroller use [33]. Similarly, unified control strategies UCS have been proposed for photovoltaic-based grid-connected voltage source converters, aiming to optimize system performance under diverse grid condition, the current work includes simulation-based studies on a 2 kVA grid-connected system under balanced grid conditions. The effectiveness of the proposed control strategy is demonstrated through these simulation results [34].

Innovations in hardware implementation have also been explored, with some articles detailing the design and implementation of GPV systems, utilizing inventive inverter designs and control algorithms, in this work, A TMS320F28335 DSP processor effectively controls the B4 inverter, leveraging its features to implement necessary control algorithms. Initially, the PV system is simulated and assessed using MATLAB/Simulink. Following this, hardware circuits are designed and implemented based on the simulation outcomes [35]. However, the validation of these systems often remains confined to simulation environments.

Fractional-order integral sliding mode control FOISMC has emerged as another promising avenue, showcasing improvements in power quality and stability in grid-connected PV systems [36]. While simulations serve as a key validation tool, practical implementations are relatively limited.

Moreover, integral backstepping control IBC techniques have garnered attention for their ability to manage power quality and optimize performance in micro-grid-connected PV systems with battery storage, demonstrating enhanced robustness and efficiency [37]. Similarly, studies have explored the interfacing of grid-connected PV systems, emphasizing efficient power extraction and transfer using MPPT and voltage source inverters [38].

Finally, microcontroller-based sine wave inverters have been developed for GPV systems, ensuring efficient power transfer and synchronization with the grid [39]. These implementations often rely on cost-effective reconfigurable boards, showcasing their potential for practical applications.

In contrast to the predominantly studies outlined above, our article stands out by presenting a hardware prototype of a three-phase grid-connected inverter. Leveraging the Arduino DUE microcontroller platform, we implement various control algorithms, including synchronization, SVPWM, and current control. This practical demonstration not only validates the efficacy of our proposed hardware solution but also underscores its potential for real-world applications, overcoming the limitations of simulation-based approaches. Additionally, by utilizing a cost-effective reconfigurable board like Arduino DUE, our work offers a scalable and affordable solution for GPV systems, enhancing accessibility and feasibility in deployment. Furthermore, the availability of our hardware prototype can serve as a valuable resource for future researchers, facilitating the validation of their simulation approaches and fostering advancements in the field of GPV systems. We acknowledge that all the presented articles are important in terms of research, and we do not seek to diminish their value. Each one makes a significant contribution to the field of GPV systems in various ways.

3. CIRCUIT TOPOLOGY AND MAIN COMPONENTS OF THE PV SYSTEM CONNECTED TO THE GRID

The main requirements for GPV systems are to convert the DC voltage generated by solar panels into AC voltage suitable for grid connection. This involves using DC-DC converters to increase the DC voltage before converting it to AC with inverters. The output voltage and frequency of the inverter must match the grid's, a synchronization algorithm is used for this purpose. The control system must adapt to weather conditions, utilizing MPPT algorithm to maximize power extraction. The DC-DC converter focuses on voltage increase and MPPT, while the inverter ensures proper power injection and synchronization with the grid [40]. In addition to the three-phase inverter, the LCL filter is used to minimize the high THD value. The GPV system block diagram is depicted in Figure 1. Therefore, the proper selection of the components parameters is very important, including:

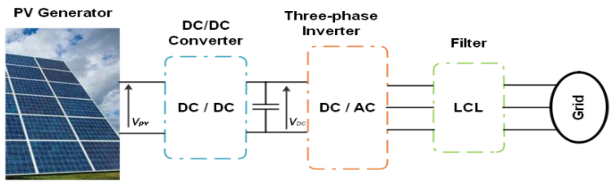

Figure 1. Grid-connected PV system diagram

3.1 Solar panel and MPPT control

Solar energy from photovoltaic (PV) panels is expected to be a major player in our future energy mix. The cost of PV modules has dropped significantly in the last decade, leading to the widespread establishment of large-scale PV power plants in many countries. Despite these advancements, the cost per unit of PV energy remains higher than that of fossil fuels. This has spurred intensive research efforts aimed at boosting the efficiency of PV systems, particularly by enhancing the

performance of solar cells.

One effective strategy for improving PV system efficiency involves optimizing the components that make up the system, especially the power converter. A promising area for improvement is the development of more efficient MPPT algorithms. These algorithms, implemented through software in the power converter's firmware, can enhance performance without requiring additional hardware investment. They work by dynamically adjusting the operating voltage or current to maximize power output based on real-time environmental conditions like sunlight intensity and temperature fluctuations. However, this task is complex because environmental factors are constantly changing, and the relationship between PV panel output and environmental conditions is nonlinear. As a result, achieving optimal MPPT performance remains a significant challenge in the quest to maximize the efficiency of PV systems.

The proposal for an improved P&O MPPT algorithm aimed at eliminating power oscillations and ensuring that the operating point does not deviate from its tracking location was previously published [41, 42]. For more details, please refer to it.

3.2 Three-phase grid-connected inverter

3.2.1 Theory of the three-phase inverter

The Voltage Source Inverter (VSI) converts DC to AC voltage and is classified into single-phase and three-phase types. This paper focuses on three-phase VSIs, used for medium to high-power applications to provide a balanced source of three-phase voltages. Figure 2 shows that the inverter consists of three switching arms, each with two cells containing a diode and a transistor, operating in forced commutation.

In controllable mode, the inverter arm acts like a two-position switch, allowing two different voltage levels at the output. It's crucial that the switches in any inverter arm (S1 and S4, S2 and S5, or S3 and S6) are not activated at the same time, as this would cause a short circuit in the power supply. Similarly, both switches in an inverter arm should not be turned off at the same time. Table 1 shows the eight valid switching states for a standard three-phase VSI setup [43].

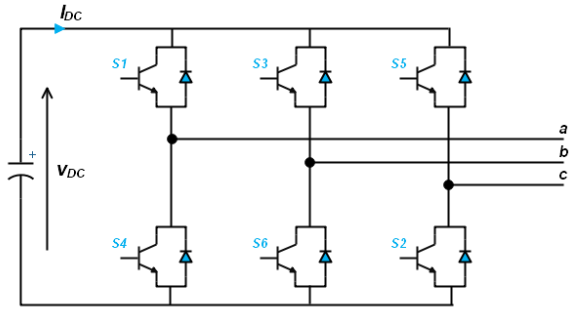

Figure 2. Three-phase inverter topology

Table 1. Switch states for a three-phase VSI

Transistor Statue	State No.	Switch States	Vab	Vbc	Vca
S1, S2, and S6 are ON	1	100	VDC	0	-VDC
S2, S3, and S1 are ON	2	110	0	VDC	-VDC
S3, S4, and S2 are ON	3	010	-VDC	VDC	0
S4, S5, and S3 are ON	4	011	-VDC	0	VDC
S5, S6, and S4 are ON	5	001	0	-VDC	VDC
S6, S1, and S5 are ON	6	101	VDC	-VDC	0
S1, S3, and S5 are ON	7	111	0	0	0
S4, S6, and S2 are ON	8	000	0	0	0

3.2.2 Mathematical modeling of the three-phase inverter

The electrical behavior of the inverter in the stationary reference frame (abc) can be expressed as follows [36]:

$$\begin{bmatrix} u_a \\ u_b \\ u_c \end{bmatrix} = R \begin{bmatrix} I_a \\ I_b \\ I_c \end{bmatrix} + L \frac{d}{dt} \begin{bmatrix} I_a \\ I_b \\ I_c \end{bmatrix} + \begin{bmatrix} v_a \\ v_b \\ v_c \end{bmatrix} \quad (1)$$

where, v_{abc} are the output voltages of the inverter connected to the grid, i_{abc}, are the three-phase grid currents, are the three-phase grid voltages, L and R are respectively, the inductor and the resistance, between the grid and the inverter connected to the grid. Using the Park transformation, we can construct Eq. (1) to simplify the model of the three-phase inverter. Eq. (2) provides the inverter output voltages in the synchronous reference frame (dq).

$$\begin{bmatrix} v_d \\ v_q \end{bmatrix} = L \frac{d}{dt} \begin{bmatrix} I_d \\ I_q \end{bmatrix} + R \begin{bmatrix} I_d \\ I_q \end{bmatrix} + \omega L \begin{bmatrix} -I_d \\ I_q \end{bmatrix} + \begin{bmatrix} u \\ u_q \end{bmatrix} \quad (2)$$

3.2.3 Three-phase grid-connected inverter control strategy

The operation of a three-phase inverter relies on Pulse Width Modulation (PWM) algorithms to control switch activation, thereby generating the desired output voltage. Over the years, extensive research has led to the development of various PWM techniques, each tailored to specific machine types, power levels, and semiconductor components in power converters. While sinusoidal PWM has been historically prominent, the emergence of microprocessors has popularized Space Vector Modulation (SVM) as a fundamental approach in modern three-phase power conversion systems [44].

SVM offers numerous advantages over other techniques. This approach is based on approximating an overall control vector throughout a modulation period TPWM instead of doing separate calculations for each arm of the inverter. For a two-level three-phase inverter, there are eight distinct states, each determining a space vector. The collection of all vectors forms a hexagonal axis and divides the entire space into six sectors, numbered from 1 to 6, as depicted in Figure 3. A reference voltage vector rotates within the space vector diagram. For any given position, the reference vector can be approximated by three nearest stationary vectors, allowing the generation of gating signals for the inverter switches. Consequently, as the reference vector completes one rotation, the inverter output voltage undergoes one fundamental cycle. The subsequent sections will explain the general principles and the method for calculating the various parameters of the SVPWM [45]:

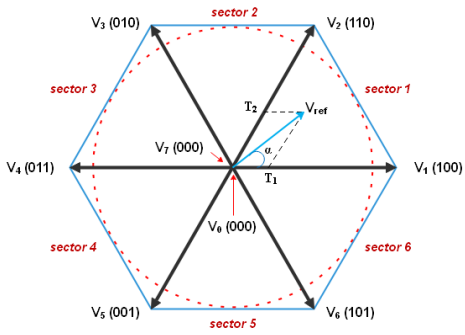

Figure 3. Space vector hexagon

a. General principle

Any two consecutive non-zero vectors have an angle of 60°. SVM is a method of digital modulation aimed at finding a combination of active and zero vectors to determinate a given reference voltage. In SVM, the three-phase voltages are mapped into the orthogonal two-phase complex reference frame $\alpha\beta$. This is known as the Clarke Transformation, as presented in Eq. (3). Then, the reference voltage ($Vref$) is used to calculate the angular frequency θ by the following equations.

$$\begin{bmatrix} V_\alpha \\ V_\beta \end{bmatrix} = \begin{bmatrix} 1 & \frac{-1}{2} & \frac{-1}{2} \\ 0 & \frac{\sqrt{3}}{2} & \frac{-\sqrt{3}}{2} \end{bmatrix} \begin{bmatrix} v_a \\ v_b \\ v_c \end{bmatrix} \tag{3}$$

hence,

$$V_{ref} = \sqrt{V_\alpha^2 + V_\beta^2} \tag{4}$$

$$\theta = \tan^{-1} \frac{V_\beta}{V_\alpha} \tag{5}$$

b. Reference space-vector locating

The second part of the SVPWM calculation involves identifying the sectors, and region to which the reference vector belongs. The sector number is identified according to the flowchart presented in Figure 4.

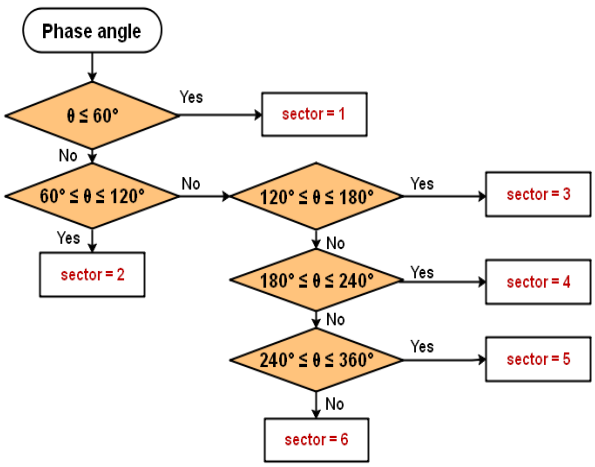

Figure 4. Sector identification

c. Switching time calculation

In this step, the calculation of the modulation index (m) as well as the dwell times (where n is the sector number ranging from 1 to 6) is performed according to Figure 4 and the following equations:

$$m = \frac{V_{ref}}{U_{DC}/2} \tag{6}$$

$$\begin{aligned} T_1 &= \frac{\sqrt{3}}{2} T_{pwm}\, m\, \sin\left(\frac{\pi}{3} - \theta\right) \\ T_2 &= \frac{\sqrt{3}}{2} T_{pwm}\, m\, \sin(\theta) \\ T_0 &= T_{pwm} - T_1 - T_2 \end{aligned} \tag{7}$$

where, m is the modulation index, UDC is the available DC voltage, T_{pwm} is the sampling period, and θ the grid phase angle extracted by the PLL algorithm.

d. Switching sequence generation

Once the dwell times are computed, the SVPWM pulses are generated. The sequence of switch activations is carefully arranged to minimize transitions between vectors, which effectively lowers the switching frequency and decreases harmonic distortions. In the initial sector, the sequence 01277210 is employed for symmetry considerations, as illustrated in Figure 5.

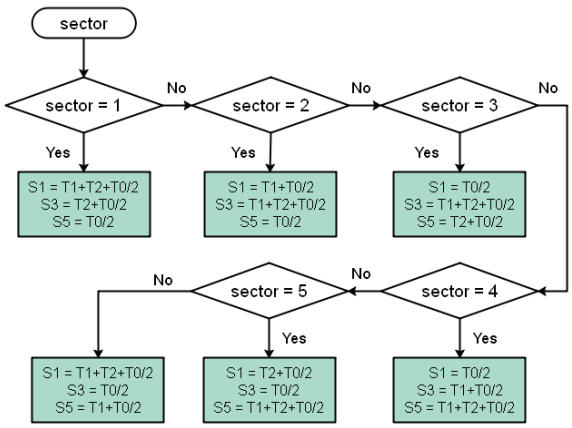

Figure 5. Switching signals identification

3.2.4 Synchronization technique

The output voltage of the inverter must be in sync with the grid voltage for PV systems that are linked to it. Finding the grid voltage's phase angle at the point of common coupling is the aim of the synchronization procedure. This helps in setting current or voltage references for active/reactive power control and harmonic current compensation. Detecting the grid phase angle is vital for controlling grid-connected inverters, and synchronization algorithms need to respond swiftly to changes in the electrical grid. They also need to filter out noise and harmonic components, especially when currents absorbed by the load are unbalanced, which can create a reverse voltage system.

Several synchronization algorithms are designed to extract the phase angle of the grid voltage, with the most common methods being zero-crossing detection, grid voltage filtering, and the phase-locked loop (PLL) technique. Zero-crossing detection, the simplest method, identifies when the grid

voltage crosses zero, providing phase and frequency information. However, it has limitations such as a low dynamic response and vulnerability to noise and harmonics, making it unsuitable for applications requiring precise and continuous phase angle detection.

Grid voltage filtering is another method for detecting the phase angle but requires additional filtering to achieve accurate phase angle and frequency detection, especially with distorted network voltage. However, the use of filters can introduce a phase shift, rendering this technique unsuitable for grid-connected inverter applications.

Our research adopts the phase-locked loop method for synchronization. Widely applied in communication technologies, PLL ensures synchronized output signals with reference inputs in both frequency and phase. Its primary aim is to adjust inverter current frequency to maintain temporal alignment with grid voltage, even amidst noise or harmonic components. Compared to other methods, PLL offers reliable frequency detection. Its fundamental functional diagram, presented in Figure 6, comprises a phase detector (PD), loop filter (LF), and phase angle detector (PD), also known as a voltage-controlled oscillator (VCO) [46].

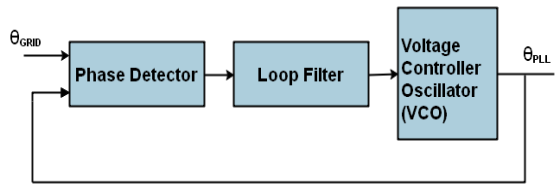

Figure 6. Phase locked loop diagram

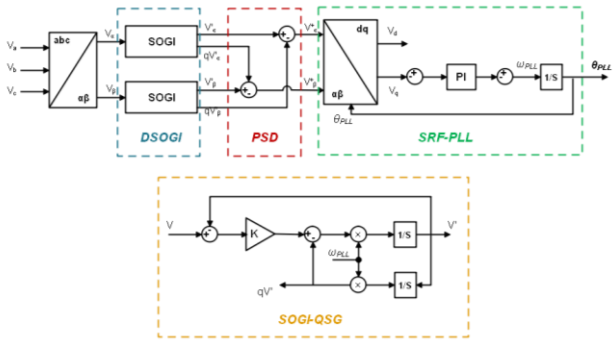

Figure 7. DSOGI-PLL block diagram

There are several PLL synchronization algorithms in the literature. It is important to note that a comparison of the most commonly used PLL synchronization algorithms has already been conducted and published in a previous work. This published study evaluated several algorithms based on criteria such as the accuracy of phase angle detection, robustness against harmonic disturbances and noise, and the speed of dynamic response. For more details on the comparison methodology and the results obtained, please refer to this published work. This information provides a solid basis for selecting the most efficient algorithm, which is used in our GPV system prototype.

Research has shown that the most suitable algorithm for our prototype is the DSOGI-PLL. Its diagram is depicted in Figure 7. Its implementation using a programmable board will be presented in the following section.

3.3 Inverter control

Two primary techniques are used to control three-phase VSI inverters: voltage control and current control. To regulate power flow, a voltage-controlled inverter modifies the phase angle between the grid voltage and the inverter's output voltage. Conversely, a current-controlled VSI utilizes pulse width modulation (PWM) techniques to regulate the active and reactive components of the current delivered to the grid. Current control methods provide faster response times and are less influenced by voltage phase shifts and grid voltage distortions. In contrast, voltage control methods are more sensitive to minor phase errors, which can lead to significant harmonic currents. Therefore, current control is preferred for grid-connected inverter management [47].

The PI (Proportional-Integral) controller is the most popular technique for current control in inverters, effectively minimizing the error between the measured output and desired grid current. It employs proportional (Kp) and integral (Ki) constants to ensure an excellent steady-state response, stable switching frequency, and accurate harmonic control. PI controllers are robust and do not require a system model. They can operate in both stationary (αβ) and synchronous (dq) reference frames, with the synchronous frame preferred for its ability to eliminate steady-state error, making it ideal for grid-connected three-phase inverters.

According to the detailed mathematical model of the inverter presented earlier, the inverter output voltages in the dq frame are given by Eq. (2) [48]. By rearranging the equation, we can find that:

$$\begin{Bmatrix} L\frac{di_d}{dt} + R\, i_d = v_d - u_d + \omega L i_q \\ L\frac{di_q}{dt} + R\, i_q = v_q - u_q + \omega L i_d \end{Bmatrix} \tag{8}$$

therefore,

$$\begin{aligned} \hat{V}_d &= v_d - u_d + \omega L i_q \\ \hat{V}_q &= v_q - u_q + \omega L i_d \end{aligned} \tag{9}$$

PI-type current controllers can be used to guarantee that the output currents follow the reference currents. In this instance, the following formula yields the output voltages of the current controllers:

$$\begin{cases} \hat{V}_d = k_p(i_d^* - i_d) + k_i \int (i_d^* - i_d)dt \\ \hat{V}_q = k_p(i_q^* - i_q) + k_i \int (i_q^* - i_q)dt \end{cases} \tag{10}$$

The reference voltage of the d-axis and the q-axis are expressed as follows:

$$\begin{Bmatrix} v_d^* = u_d - \omega L i_q + \hat{V}_d \\ v_q^* = u_q + \omega L i_d + \hat{V}_q \end{Bmatrix} \tag{11}$$

As illustrated in Figure 8, the block diagram of the synchronous regulator for the grid-connected inverter is derived from Eq. (11).

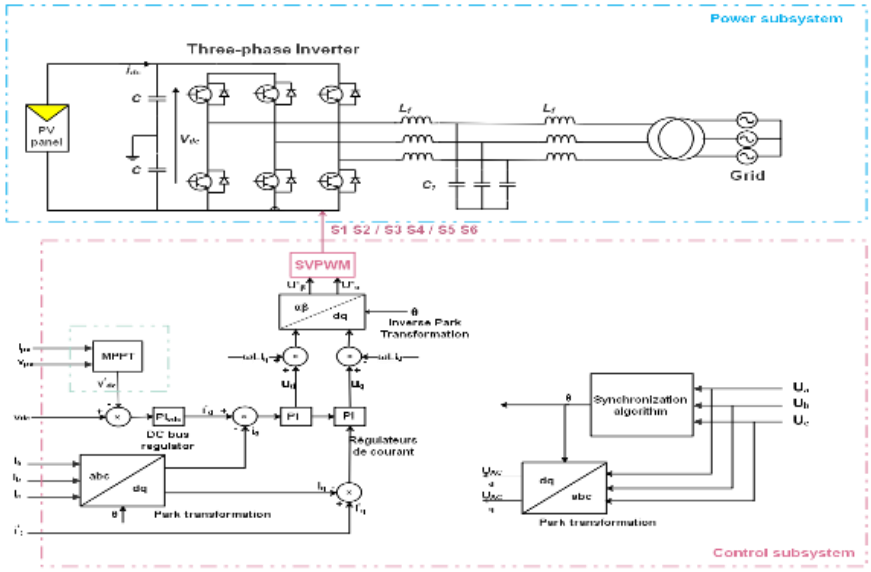

Figure 8. DSOGI-PLL block diagram

It should mention that PI (Proportional-Integral) controllers are a standard approach in current control strategies due to their simplicity and effectiveness. However, they also have limitations, particularly in dealing with non-linearities and varying system dynamics, which can lead to performance issues such as overshoot and prolonged settling times. To enhance the control performance, future improvements could explore adaptive control techniques that adjust parameters in real-time, or intelligent control strategies, like fuzzy logic or model predictive control [49], which can better handle uncertainties and nonlinear behaviors in renewable energy systems.

3.4 LCL filter

To choose an optimal filter topology suitable for the inverter in our GPV conversion system, parameters such as efficiency, weight, and volume must be considered. The LCL filter was chosen for our design due to its superior attenuation of inverter switching harmonics compared to other topologies. The main advantages of the LCL filter, as highlighted [50]:

• Minimizing grid distortion and reactive power generation;

• Providing -60 dB/decade attenuation for frequencies above the resonance point;

• Allowing operation at a relatively low switching frequency while maintaining effective harmonic attenuation;

Its performance is not affected by variations in grid im • pedance.

• The single-phase electrical diagram of this filter, depicted in Figure 9, is considered for its modeling. The circuit and components are identical for the other two phases.

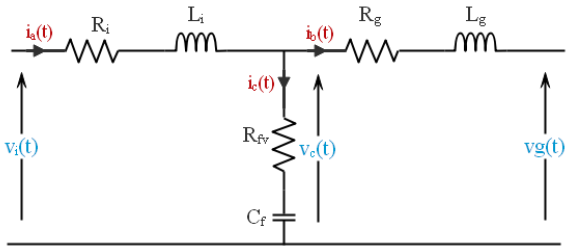

Figure 9. LCL single-phase electrical diagram

Using Kirchhoff's law, the equations of the filter can be written as follows:

$$\begin{aligned} i_a - i_b - i_c &= 0 \\ v_i - v_c &= i_a(sL_i + R_i) \\ v_c - v_g &= i_b(sL_g + R_g) \\ v_c &= i_c(\frac{1}{sC_f}) \end{aligned} \tag{12}$$

According to research, the LCL filter produces a resonance peak at its cutoff frequency, potentially causing system instability. To address this, passive damping is added using a virtual resistance R_{fv}, which reduces the voltage across the capacitor proportionally to the current through it. This improves the filter's simplicity, reliability, and efficiency. Among the possible placements for the resistance (series/parallel with the inverter-side inductance or filter capacitor), the series connection with the filter capacitor was chosen.

The equations of the filter then become as following:

$$\begin{aligned} i_a - i_b - i_c &= 0 \\ v_i - v_c &= i_a(sL_i + R_i) \\ v_c - v_g &= i_b(sL_g + R_g) \\ v_c &= i_c(\frac{1}{sC_f} + R_{fv}) \end{aligned} \tag{13}$$

4. DESIGN PROCEDURE OF THE GRID-CONNECTED PV SYSTEM

This section outlines the development of a laboratory-scale test prototype for a GPV conversion system at reduced power. It details the experimental implementation of the system using the Arduino DUE board as a cost-effective approach, yielding significant results suitable for GPV projects. Additionally, the section explains the theoretical considerations and implementation approach necessary for the successful integration of the proposed grid-connected inverter system. It emphasizes the interdisciplinary knowledge required, spanning electrical and computer engineering domains.

The prototype of the complete PV system test is illustrated in Figure 10. A thorough search was conducted to select the appropriate circuit components for its implementation. Key factors determining the project components include performance, effectiveness, size, and, of course, cost. The overall system comprises two main parts: a power section and a control section. The former consists of the three-phase inverter and the power supply circuit, which includes a three-phase input source to power the two-level three-phase inverter. The latter contains the Arduino DUE control board with its operating software.

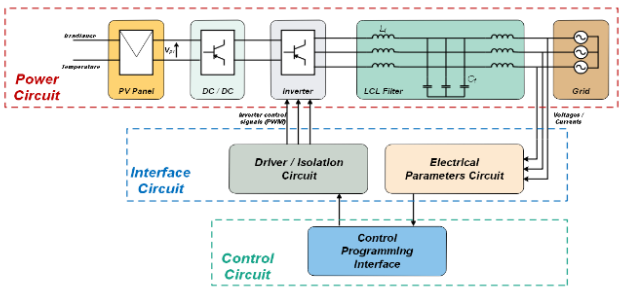

Figure 10. Block diagram of the proposed grid-connected PV system

The two sections mentioned above require an intermediate interface consisting of a driver circuit for the transistors constituting the inverter arms, optocouplers for isolation, and signal measurement sensors. Each part is described in detail in the next three sections.

4.1 Power circuit

4.1.1 Overall power circuit design

Each inverter arm consists of two power N-channel MOSFETs, IRF840, with a drain-source resistance of 0.85 ohms and capable of handling up to 500V and 8A. The high-side drain terminals of N-channel MOSFETs are frequently connected when switching a DC voltage across a load because the MOSFET requires a gate terminal that is around 10V higher than the drain terminal in order to conduct. Integrated circuit devices referred to as "MOSFET drivers" are frequently employed in conjunction with charge pumps or bootstrap methods to provide this voltage differential. The ensuing subsections will provide more information on these circuits.

4.1.2 Three-phase inverter transistor design

The MOSFET transistor selected for our experimental application supports 500V at its terminals and a current of 8A. This transistor is sensitive to abrupt changes in voltage and current that occur during switching. Hence, two commutation aid circuits (known as CALC or Snubber) must be added to the closing and opening states of the switch.

a. Protection against high di/dt during the MOSFET transistor's closure

Semiconductors are highly sensitive to abrupt changes in voltage and current that occur during switching. To counteract current variations and prevent current surge before complete voltage cancellation across the MOSFET, an inductance is employed to delay the current. Additionally, to dampen the oscillations induced by the inductance L and dissipate the energy stored by the inductor during the off-state, a commutation aid circuit (CALC or Snubber) or softener is inserted, as shown in Figure 11, using a resistor R and a Flyback diode. There are two design constraints for the series CALC circuit when the switch is closed:

• The overvoltage across the switch must be equal to R/Ik.

• The discharge time of the inductance must be less than the transistor switching time: $t1 = 3L/R$, where $L = Vk\ tr/Ik$, where, $t1$ is the initialization or discharge time of the inductance L; tr is the response time of the MOSFET switch; Vk and Ik are the voltage and current ratings of the MOSFET switch; R and L are the resistance and inductance of the CALC at the closed state.

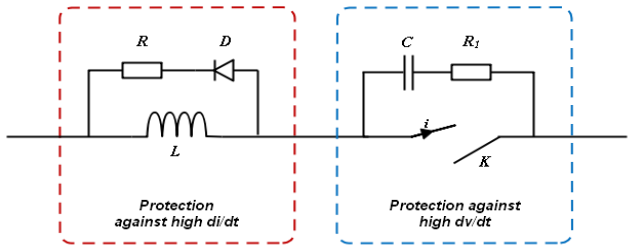

Figure 11. Commutation aid circuit

b. Protection against high dv/dt during the opening of the MOSFET transistor

To mitigate over voltages during the opening of the MOSFET transistor, a CALC circuit consisting of an RCD circuit in parallel with the switch is inserted. This circuit serves to slow down the voltage buildup across the switch until the current is completely zero. An additional nonlinear element, the diode, placed in parallel with the element or at the head of the installation, dissipates the energy of the overvoltage by limiting the voltage growth and diverting part of the current, as shown in Figure 11.

The resistor limits the discharge of the capacitor in the switch when it is closed. The parallel CALC circuit, like the previous one, adheres to two constraints:

• Overcurrent on the switch is set equal to $Vk/R1$.

• The discharge time of the CALC capacitor must be less than the transistor's switching time: $t2 = 3R1 * C$, where $C = 4/9*(Ik\ tf)/2Vk$, where $t2$ is the discharge time of capacitor C, tf is the MOSFET switch decay time, $R1$, and C are respectively the resistance and capacitance of the CALC circuit.

c. Thermal protection

In normal operation, the PN junction runs the risk of reaching a too high temperature ($\theta jmax$ given by the manufacturer). To address this issue, the component is mounted on a heat sink or "radiator" to ensure the dissipation of thermal energy. After calculating the maximum power dissipated by the component (using its equivalent circuit: $fcem$ or ({$fcem$ + resistance}), one can calculate the thermal resistance of the heat sink to be installed.

4.2 Interface circuit

4.2.1 MOSFET driver

The MOSFET is a voltage-controlled device that requires a minimum switching threshold of about 15V. The output signal values from the Arduino are not sufficient for MOSFET operation. Therefore, a control driver known as the "MOSFET Driver" must be used, capable of quickly charging the MOSFET's input capacitance before the potential difference is reached.

By translating low-voltage control signals (output from the Arduino DUE) into voltages capable of delivering sufficient gate voltage (15V), a variety of MOSFET drivers are available to power N-channel MOSFETs. The IR2111 circuit is chosen for our implementation;

The IR2111 drivers facilitate the translation of 3.3V logic signals from the control board to the operational voltage level required by the power MOSFETs. Controlled by PWM signals, the IR2111 manages switching through the HI and LI pins, with HI controlling the high-side output (HO) and LI controlling the low-side output (LO). The SD pin governs device shutdown, connected to the Arduino, while the VDD pin is linked to 5V for biasing purposes. External connections include the VSS pin to ground and the VCC pin to 15V. In a three-phase setup, three IR2111 devices are utilized, as illustrated in Figure 12, with each device requiring connections to bootstrapping components. Figure 12 illustrates a connection scheme for a single IR2111 device.

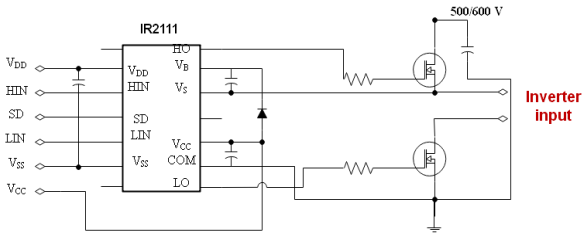

Figure 12. Single IR2111 typical connection scheme

As depicted in Figure 12, the essential external components needed for the IR2111 to operate are the capacitor and bootstrap diode. The capacitor supplies gate drive to the high-side MOSFET through the bootstrap diode. This setup allows the capacitor to maintain a voltage difference that rapidly switches the MOSFET to full activation. Eq. (14) is utilized to calculate the appropriate values for these components.

$$C \geq \frac{2\left[2Q_r + \frac{I_{crmax}}{F}\right] + Q_{ls} + \frac{I_{c(leak)}}{F}}{V_{cc} - V_c - V_{ls} - V_{MIN}} \qquad (14)$$

Table 2. Eq. (14) parameters

Component	Label	Value
Gate charge of the high-side MOSFET	Qr	41 nC
Quiescent current for the high-side driver circuit	Icr	230 Ma
Charge level required per cycle	Qls	5nC
Bootstrap capacitor leakage current	Ic(leak)	250 µA
Frequency	f	50 Hz
Supply voltage	Vcc	15V
Voltage drop across the bootstrap diode	Vc	1V
Voltage drop on the low side	Vls	1.5V

The elements of the Eq. (14) can be found in the datasheets as presented in Table 2.

Based on the calculations, a 10 μF bootstrap capacitor is selected. To minimize the charge return from the capacitor to the VCC supply, a fast recovery diode, specifically the 4N25, is used. Additionally, a PC817 optocoupler is employed to isolate the control circuit from the power section.

4.2.2 Electrical parameter acquisition circuit

A measuring board is necessary to monitor the injected grid current as well as the three-phase grid voltage in order to enable control. The circuits for the voltage and current sensors will be covered in separate sections that follow.

a. Voltage sensor

This circuit is designed to measure the voltages of the three-phase grid. Hence, the ZMPT101B voltage sensor module was chosen for use. It is a hall effect voltage sensor made from the ZMPT101B voltage transformer. It can measure up to 250V AC with high precision and good consistency for voltage and power measurement. Its operation is straightforward and relies on a potentiometer for adjusting the ADC output.

The operating principle of this sensor is as follows: the three voltages of the electrical grid, which ideally vary sinusoidally between -220 √ 2 and 220 √ 2 V, need to be converted into three sinusoidal signals, with the same frequency, ranging from 0 to 3.3V. This transformation was achieved using three ZMPT101B voltage sensors [51]. The sinusoids from 0 to 3.3V serve as input to the Arduino DUE. Thus, theoretically, when, at a certain moment, the grid voltage is, for example, 0V, the Arduino will read 1.6V on the corresponding analog input, and if the grid voltage is equal to 220 √ 2, the Arduino will read 3.3V on its input.

b. Current sensor

A current sensor is a transducer that produces a voltage image of the measured current. The current sensor chosen for our experimental setup is the ACS712 30A sensor. This sensor is connected in series with the load in an alternating current (AC) or direct current (DC) circuit and allows for the measurement of the current flowing through the sensor.

The device features an accurate, low-offset linear Hall effect system with a copper conduction path on the chip's surface. As current flows through this path, it generates a magnetic field, which the integrated Hall circuit detects and converts into a proportional voltage. The sensitivity of this system is 0.066V/A (66mV per ampere). This voltage can then be read on an analog input of the Arduino, and subsequently, using mathematical equations, obtain the corresponding current value (in amperes). It is also important to perform an open-loop measurement (without current) to obtain the calibration value Vref of the module (which should be VCC/2, i.e., 2.5V).

4.3 Control circuit

The control circuit's function is to carry out the control loop. Figure 13 shows the grid-connected inverter's control arrangement. The grid voltage and the current fed into the grid are first detected, as this figure illustrates. The DSOGI-PLL algorithm then extracts the grid angle. The current control loop is then run through a PI regulator. Finally, the vector PWM modulation technique is executed, and the switching signals for the power converter are generated. The design of the inverter control involves two important parts: hardware and software. The hardware design centers on the control board, which incorporates the Arduino DUE. On the software side, the control algorithms are developed and implemented using the Arduino IDE.

4.3.1 Control hardware for the grid-connected inverter

The Arduino DUE, utilized for control purposes, is built on the Atmel SAM3X8E ARM Cortex-M3 processor featuring a 32-bit ARM microcontroller. It is programmed via the Arduino Software (IDE) and offers 54 digital input/output pins. The DUE's 12 PWM output pins facilitate the generation of

multiple synchronized pulse width modulation signals.

In general, this board was chosen for use in the experimental part of this research due to its low cost compared to other electronic devices, its performance, and its size, which facilitates the design of the overall system. Specifically, the DUE was chosen because, like other Arduino boards, it has an integrated development environment (IDE) that greatly simplifies coding, program uploading, and debugging. Additionally, among the Arduino boards available on the market, the DUE is the only one with the highest processing capacity and features 2 analog output pins capable of handling up to 12-bit resolution, totaling 4096 distinct voltage levels in the range of 0 to 3.3 V, which generates a resolution of 0.8 mV.

4.3.2 Software for grid-connected inverter

The main process specific to the control of the three-phase grid-connected inverter is depicted in the control flowchart of the system provided in Figure 13.

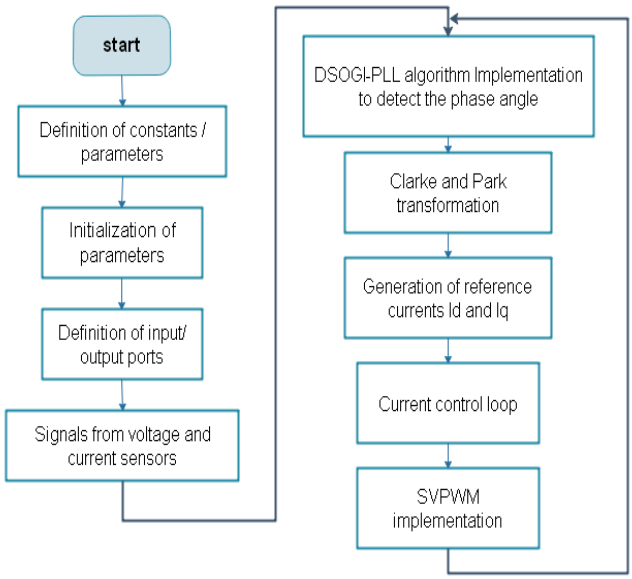

Figure 13. Grid-connected PV system global flowchart

1. Implementation of the synchronization strategy

The DSOGI-PLL algorithm used in this research determines the phase angle of the grid voltage by detecting the symmetrical components of the positive sequence of the grid [52]. The positive sequence $vabc+$ of the balanced three-phase grid $vabc$ can be obtained from the voltages composing the original system as shown in Eq. (15). Then, by applying the Clarke transformation, we obtain the coordinates of the three-phase system in the αβ reference frame, as presented in Eq. (16). Based on these two equations, a new transformation can be deduced to obtain the positive sequence in the αβ reference frame, as shown in Eq. (17):

$$v_{abc}^{+} = \begin{bmatrix} v_a^{+} \\ v_b^{+} \\ v_c^{+} \end{bmatrix} = T_{+} v_{abc} = \frac{1}{3}\begin{bmatrix} 1 & a^2 & a \\ a & 1 & a^2 \\ a^2 & a & 1 \end{bmatrix}\begin{bmatrix} v_a \\ v_b \\ v_c \end{bmatrix} \quad (15)$$

$$v_{\alpha\beta} = \begin{bmatrix} v_\alpha \\ v_\beta \end{bmatrix} = T_{\alpha\beta} v_{abc} = \frac{2}{3}\begin{bmatrix} 1 & \frac{-1}{2} & \frac{-1}{2} \\ 0 & \frac{\sqrt{3}}{2} & \frac{-\sqrt{3}}{2} \end{bmatrix}\begin{bmatrix} v_a \\ v_b \\ v_c \end{bmatrix} \quad (16)$$

where, $q = e^{\frac{-j\pi}{2}}$.

$$\begin{aligned} v_\alpha^{+} &= \frac{1}{2}(v_\alpha - q v_\beta) \\ v_\beta^{+} &= \frac{1}{2}(v_\alpha + q v_\beta) \end{aligned} \quad (17)$$

Based on the previous equations, we can conclude that for the calculation of the positive sequence, the voltages of the original system and their corresponding quadrature are necessary. To generate these signals, a second-order generalized integrator SOGI is used, as shown in Figure 7. The SOGI contains an input which is the signal v, and two outputs, the signal v' resulting from the filtering of signal v, and the signal qv', corresponding to the filtered signal and in quadrature with v'. It is also possible to deduce the transfer functions that connect the input to the two outputs (Eq. (18) and Eq. (19)).

$$D(s) = \frac{v'}{v}(s) = \frac{k\,\omega' s}{s^2 + k\,\omega' s + \omega'^2} \quad (18)$$

$$D(s) = \frac{qv'}{v}(s) = \frac{k\,\omega'^2}{s^2 + k\,\omega' s + \omega'^2} \quad (19)$$

The synchronization method must be reformulated and structured into a programming language recognized by the DUE. To do this, we need to obtain its mathematical model in discrete time.

The continuous-time mathematical model of the SOGI module is expressed by the transfer functions in Eq. (18) and Eq. (19).

To discretize the SOGI, the bilinear transformation [53] (also known as the Tustin method or trapezoidal transformation) has been used. By applying this transformation to Eq. (18) and Eq. (19), and rearranging the resulting terms, we obtain the mathematical model of the SOGI in real time (Eq. (20)).

$$\begin{aligned} \frac{v'(z)}{v(z)} &= \frac{\frac{2k\omega'}{T}(z^2-1)}{\left(\frac{2k\omega'}{T}+\frac{4}{T^2}+\omega'^2\right)z^2+\left(2\omega'^2-\frac{8}{T^2}\right)z+\frac{4}{T^2}+\omega'^2-\frac{2k\omega'}{T}} \\ \frac{qv'(z)}{v(z)} &= \frac{k\,\omega'^2\,(z^2+2z+1)}{\left(\frac{2k\omega'}{T}+\frac{4}{T^2}+\omega'^2\right)z^2+\left(2\omega'^2-\frac{8}{T^2}\right)z+\frac{4}{T^2}+\omega'^2-\frac{2k\omega'}{T}} \end{aligned} \quad (20)$$

Then, by applying the inverse z-transform to Eq. (20) and isolating the resulting terms v' $(k+2)$ and qv' $(k+2)$, we obtain the following equation:

$$\begin{aligned} v'(k+2) &= \frac{\left(\frac{8}{T^2}-2\omega'^2\right)v'(k+1)+\left(\frac{2k\omega'}{T}-\frac{4}{T^2}-\omega'^2\right)v'(k)+\frac{2k\omega'}{T}[v(k+2)-v(k)]}{\frac{2k\omega'}{T}+\frac{4}{T^2}+\omega'^2} \\ qv'(k+2) &= \frac{\left(\frac{8}{T^2}-2\omega'^2\right)qv'(k+1)+\left(\frac{2k\omega'}{T}-\frac{4}{T^2}-\omega'^2\right)qv'(k)+k\omega'^2\,[v(k+2)+2v(k+1)+v(k)]}{\frac{2k\omega'}{T}+\frac{4}{T^2}+\omega'^2} \end{aligned} \quad (21)$$

To obtain the estimation of the positive sequence in the $\alpha\beta$ reference frame, the values of the estimated voltages v' and qv' must be added (Figure 9) according to the following equation:

$$v_\alpha^{+} = \frac{1}{2}\left(v_\alpha' - q v_\beta'\right);\; v_\beta^{+} = \frac{1}{2}\left(q v_\alpha' + v_\beta'\right) \quad (22)$$

The discretization of the dq-PLL algorithm involves

discretizing the PI controller and the integrator. Therefore, consider the continuous-time transfer function of the PI controller of the dq-PLL, as presented in Eq. (23).

$$\frac{X(s)}{V_q^+(s)} = k_p + \frac{k_i}{s} \tag{23}$$

By applying the bilinear transformation to Eq. (23), the discrete-time model of the PI controller is obtained. Subsequently, by applying the inverse z-transform, we obtain the resulting term (Eq. (24)) of the output of the PI controller.

$$x(k+1) = \left(\frac{k_i T}{2} + k_p\right) v_q^+(k+1) + \left(\frac{k_i T}{2} - k_p\right) v_q^+(k) + x(k) \tag{24}$$

To discretize the integrator of the dq-PLL, we proceed in a similar manner. The continuous-time transfer function of the integrator of the dq-PLL is presented in Eq. (25), where the input is the estimated angular frequency in radians per second, and the output is the estimated phase in radians.

$$\frac{\theta'(s)}{\Omega'(s)} = \frac{1}{s} \tag{25}$$

After applying the bilinear transformation and the inverse z-transform to the previous equation, and isolating the resulting term θ' (k+1), we obtain the formula presented below (Eq. (26)), allowing us to calculate the values of the samples of the phase angle θ' (k+1) and the angular frequency ω' (k+1) based on the directly preceding samples.

$$\theta'(k+1) = \frac{T}{2}[\omega'(k+1) + \omega'(k)] + \theta'(k) \tag{26}$$

2. Implementation of the SVPWM technique

The implementation of the SVPWM algorithm have been carried out following the steps presented earlier in section 3. The proposed algorithm is developed using the Arduino DUE board.

3. Implementation of the current control strategy

For a high-performance application requiring precise current tracking under dynamic conditions, it is advisable to use the controller scheme described earlier in section 3 for the grid-connected three-phase inverter. The output signals from the PI controllers, following the dq/abc transformations, serve as inputs to the SVM block to generate the switching pulses.

As shown in Figure 8, two identical conventional PI controllers are used. Each of them contains the proportional gain (Kp) and the integral gain (Ki). The process of tuning the optimal gains to achieve an ideal response from the control system in our application is the Ziegler-Nichols tuning method. These rules are used to provide an estimation of parameter values and provide a starting point for fine-tuning.

After calculating the parameters of the PI controllers, discretization of these controllers is performed as indicated in the previous section.

4.4 Filtering circuit

The output voltage of the three-phase inverter is a high-frequency square wave; therefore, a filter is inserted between the inverter output and the electrical grid to reduce the higher harmonics caused by the switching process. Ideally, a filter with a low cutoff frequency and high attenuation at the high switching frequency is preferred to effectively attenuate the ripples. However, the design of the filter must be a compromise between switching losses, efficiency, and fundamental voltage drop.

Based on the design presented in section 3, numerical values of the different components are chosen to design and implement an optimal filter ensuring the lowest possible Total Harmonic Distortion (THD) rate to meet the requirements of the grid effectively. The parameters of the system considered for calculating the values of the components of the LCL filter with a power of 1.5 KVA are presented in Table 3.

Table 3. The proposed system parameters

Parameter	Value
Output power of the three-phase inverter	$S_n = 1.5$ KVA
Phase voltage of grid	$E_{ph} = 220$ V
Grid frequency	$f = 50$ Hz
Switching frequency of the MOSFETs	$f_{switch} = 5$ KHz
DC link voltage	$V_{DC} = 100$V

The base impedance and capacitance are defined by Eq. (27) and Eq. (28), respectively:

$$z_b = \frac{(E_c^2)}{S_n} \tag{27}$$

$$c_b = \frac{1}{\omega z_b} = 0.33\ [\mu F] \tag{28}$$

By taking the maximum variation of the power factor from the grid's perspective equal to 5%, we can determinate the value of the filter capacitance (Eq. (29)).

$$C_f = 0.05 * c_b = 1.6\ [\mu F] \tag{29}$$

We have chosen a ripple of 10% in order to design the parameters of the LCL filter. The maximum ripple, the maximum current, and the inverter-side inductance are presented by the following equations:

$$\Delta I_{Lmax} = 0.1 I_{max} \tag{30}$$

$$I_{max} = \frac{P_n \sqrt{2}}{3E_c} \tag{31}$$

Therefore:

$$L_i = \frac{V_{DC}}{6 f_{switch} \Delta I_{Lmax}} \tag{32}$$

By imposing an attenuation factor k_a of 20%, the value of the inductance l_g is obtained using the following equation:

$$L_g = \frac{\sqrt{\frac{1}{k_a^2}+1}}{C_f\, \omega_{switch}^2} \tag{33}$$

The resistance in parallel with the capacitance is given by Eq. (34) and serves to attenuate a portion of the ripple at the switching frequency to avoid the resonance peak.

$$R_f = \frac{1}{3\,\omega_{res}\,C_f} \tag{34}$$

with:

$$\omega_{res} = \sqrt{\frac{L_i + L_g}{L_i L_g C_f}} \tag{35}$$

Table 4 presents the numerical values of the various components of the LCL filter.

Table 4. LCL filter parameters

Parameter	Label	Value
Grid side inductance	*Lg*	3.8 mH
Inverter side inductance	*Li*	10 mH
Filtering capacitance	*Cf*	1.6 µF
Damping resistance	*Rf*	13.8 Ω

5. EXPERIMENTAL RESULTS AND DISCUSSIONS

The experimental version of the GPV system proposed in this research was implemented in our laboratory "Advanced Systems Engineering, National School of Applied Sciences Kenitra" (Figure 14 and Figure 15).

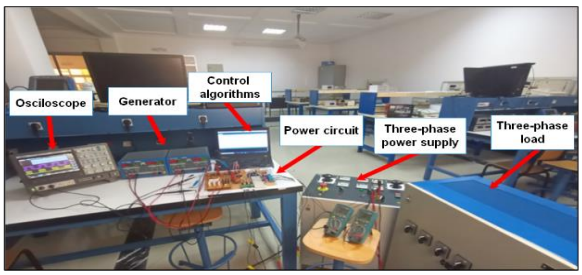

Figure 14. Experimental version of the proposed GPV system

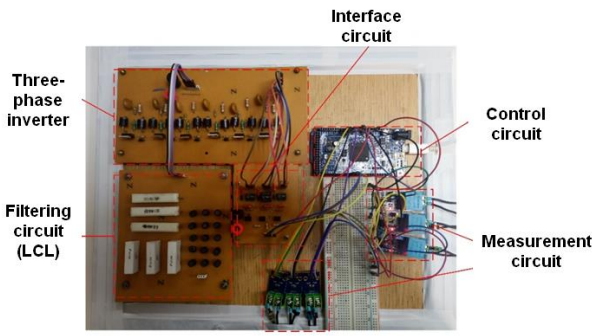

Figure 15. Power section prototype of the studied system

Due to the constraints of the laboratory facilities, the experimental model has been scaled down but still meets the intended objectives. The hardware design is validated by testing the various project components, including the three-phase power circuit, the three-phase load, the control board, the measurement board, the interface board, and the filtering board. After verifying the proper functioning of the various components through testing, this section concludes with the presentation of experimental data for grid integration.

5.1 Three-phase voltage measurement

A measurement board is required to monitor the voltage of the three-phase grid and the current fed into the grid for control purposes. The signals shown in Figure16 are the grid voltages outputted from the voltage sensor. By observing the average and maximum voltage and frequency measurements taken by the oscilloscope, it is noted that they correspond to what is expected: a sine wave in the range of 0 to 3.3 V, indicating an average voltage of nearly 1.5 V, a maximum voltage of 3.3 V (for a voltage of 250 V), and a frequency of 50 Hz.

The implemented algorithm must use the actual instantaneous values of the grid parameters. Therefore, in the developed code, voltages ranging from 0 to 3.3 V are mathematically converted to the range of -220 √ 2 to 220 √ 2 V, and calculations are performed with these values. If a certain signal needs to be visualized, it must be shifted to the range of 0 to 3.3 V within the code itself. Then, apply the desired signal to one of the output pins of the digital-to-analog converter (DAC) and connect this pin to a channel of the oscilloscope.

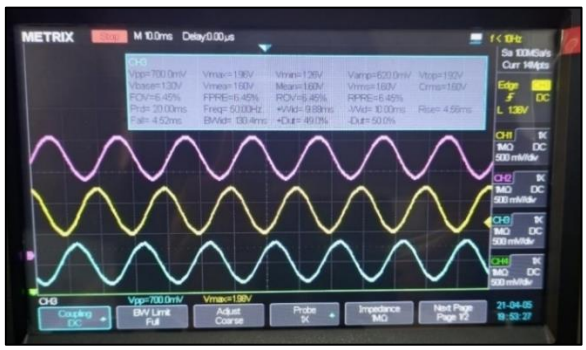

Figure 16. Grid voltages outputted from the voltage sensors

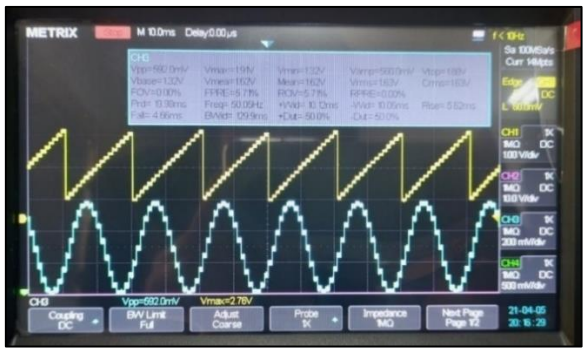

Figure 17. Temporal evolution of the PLL phase angle θPLL and the positive sequence component $v\alpha+$

5.2 Synchronization

Figure17 depicts the temporal evolution of the PLL phase angle θPLL and the positive sequence component $v\alpha+$. It is noteworthy that the frequency of both signals is approximately 50 Hz, as expected. It is also observed that the detected phase angle is synchronized with the voltage of $v\alpha+$ since the cycles of both signals start and end simultaneously. This proves that the phase angle calculated and generated by the proposed algorithm is appropriate with the phase of the input voltage; consequently, the estimated frequency is equal to the grid frequency.

5.3 SVPWM

Figure 18 provides an oscilloscope snapshot showing the temporal evolution of the phase angle and the calculated sector number.

Figure 18. Temporal evolution of the phase angle and the calculated sector number

Figure 19 and Figure 20 show a typical oscilloscope snapshot for the pulses generated after the IR2111 control circuit for driving the low-side transistors of the inverter. The pulses generated by the IR2111 control circuit are the same as the pulses generated by the Arduino board. However, their amplitude is higher.

Figure 19. Low-side transistors control signals

Figure 20. Transistors control signals

A 700 ns dead time has been incorporated between the switching pulses of each pair of complementary transistors. This interval, which is the period between turning off one transistor and turning on the other in the pair, is necessary to prevent short circuits at the DC bus level.

An example oscilloscope overview of the composite voltages of the experimental grid-connected inverter, captured just prior to the filter, is shown in Figure 21. The related simulated waveforms and the experimental waveforms are strikingly comparable. Figure 22 shows the grid voltage and the usual output voltage of the grid-connected inverter, which is obtained after the LCL filter. The output voltages of the inverter and the grid voltage are identical in frequency and phase, as the illustration makes abundantly evident.

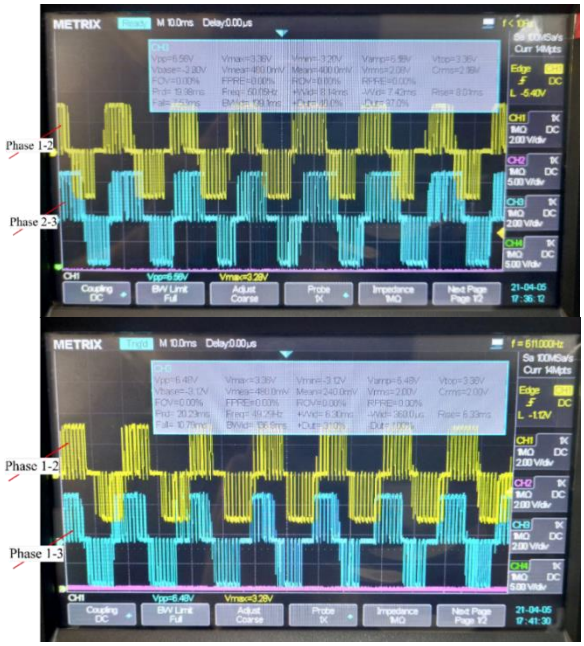

Figure 21. Experimental waveforms of the line voltages at the output of the three-phase inverter

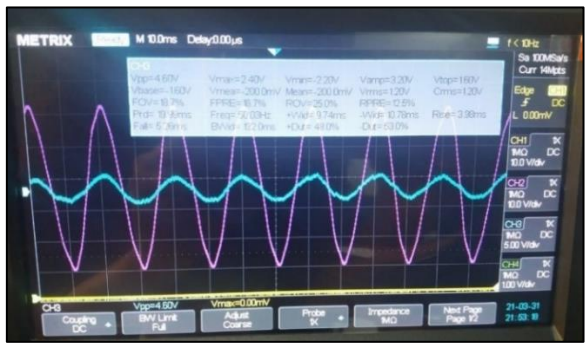

Figure 22. Grid-connected inverter voltage at the LCL filter output synchronized with grid voltage

While significant progress has been made in the field of renewable energy systems, much of the research to date remains theoretical, relying heavily on simulation-based studies, these simulations, though insightful, lack validation through real-world implementations. In contrast, our research focuses on the practical implementation of an advanced grid-connected PV system. The prototype developed in this study moves beyond theoretical analysis by offering a cost-effective, low-power hardware solution that can be tested under real conditions. Unlike simulation tools such as MATLAB/Simulink or platforms like dSPACE, which are commonly used in simulation-based studies, our hardware design relies on affordable components, making it a more viable option for large-scale deployment. By addressing the cost, size, and complexity challenges of conventional devices, this prototype paves the way for wider adoption of grid-connected PV systems.

6. CONCLUSION AND FUTURE WORK

In this paper, we extensively investigated the study, development, and implementation of three critical control aspects of the three-phase inverter: synchronization strategy, SVPWM control, and current control. Firstly, we developed a robust synchronization strategy to ensure the generated energy from the PV system is seamlessly integrated into the grid, maintaining compatibility and preventing disruptions or instability. Secondly, we employed the SVPWM strategy to effectively control the three-phase inverter. Thirdly, we focused on a precise current control strategy to uphold grid stability, prevent overloads, and ensure efficient energy transfer between the PV system and the grid.

On the hardware front, our efforts were directed towards comprehensively understanding and designing the various components of the solar PV power system. This involved measuring grid electricity, adapting commands to meet system requirements, and ensuring seamless connections between the inverter and the grid. Our evaluation of the system demonstrates the successful achievement of several key functionalities:

•The proposed DSOGI-PLL synchronization strategy ensures quick and accurate synchronization of the GPV system, even under failure conditions such as harmonic distortion, imbalance, and phase absence, significantly enhancing the dynamic performance and stability of the overall system control strategy.

•The SVPWM strategy delivers excellent performance in minimizing harmonic distortion and optimizing the control of the two-level three-phase inverter waveforms output.

•The utilization of the Arduino board for prototype realization contributes to a compact and cost-effective system design.

This laboratory-developed prototype for integrating a PV system with the electrical grid serves as a foundational platform for future researchers, enabling further improvements and validation of related research endeavors.

Overall, our work provides a comprehensive and practical approach to improving the integration and control of PV systems within electrical grids, offering valuable insights and tools for future advancements in this field.

In future research, integrating energy storage systems with renewable energy sources will be crucial for enhancing grid stability and reliability. Energy storage solutions, such as batteries or supercapacitors, can effectively manage the intermittent nature of renewable energy, allowing for smoother energy delivery and better load balancing. Furthermore, exploring advanced control algorithms, including model predictive control, adaptive control strategies, and artificial intelligence (AI), could significantly improve the performance and efficiency of renewable energy systems. These innovative approaches can optimize energy management, respond dynamically to changing conditions, and enhance overall system resilience. The incorporation of AI can facilitate real-time data analysis and decision-making.

REFERENCES

[1] Ngo, X.C., Do, N.Y. (2022). The impact of electrical energy consumption on the payback period of a rooftop grid-connected photovoltaic system: A case study from Vietnam. International Journal of Renewable Energy Development, 11(2): 581-589. https://doi.org/10.14710/ijred.2022.42981

[2] Bunda, N., Sunio, V., Palmero, S.S., Tabañag, I.D.F., Reyes, D.J., Ligot, E. (2023). Stage model of the process of solar photovoltaic adoption by residential households in the Philippines. Cleaner and Responsible Consumption, 9: 100114. https://doi.org/10.1016/j.clrc.2023.100114

[3] International Energy Agency (IEA). (2022, December 6). Renewables 2022 – Analysis. Available at https://www.iea.org/reports/renewables-2022

[4] Global Carbon Project (GCP). Global Carbon Project (GCP). https://www.globalcarbonproject.org/carbonbudget/.

[5] Rengma, N.S., Yadav, M., Kishor, N. (2023). Solar photovoltaic water pumping system: A software tool development-based optimal configuration investigation for system installation location, sizing and deployment. Renewable Energy Focus, 46: 236-255. https://doi.org/10.1016/j.ref.2023.07.001

[6] Bouthiba, Y., Meghni, B., Cherifi, A., Belhamra, A. (2024). Optimal management of a grid-connected hybrid energy system using FLC-ANN hybrid technique. Journal Européen des Systèmes Automatisés, 57(3): 849-859. https://doi.org/10.18280/jesa.570324

[7] Quansah, D.A., Adaramola, M.S., Appiah, G.K., Edwin, I.A. (2017). Performance analysis of different grid-connected solar photovoltaic (PV) system technologies with combined capacity of 20 kW located in humid tropical climate. International Journal of Hydrogen Energy, 42(7): 4626-4635. https://doi.org/10.1016/j.ijhydene.2016.10.119

[8] International Renewable Energy Agency (IRENA). (2023). Renewable Power Generation Costs in 2022. https://www.irena.org/Publications/2023/Aug/Renewable-Power-Generation-Costs-in-2022.

[9] SolarPower Europe. Global Market Outlook for Solar Power 2022-2026. https://www.solarpowereurope.org/insights/market-outlooks/global-market-outlook-for-solar-power-2022.

[10] Aarich, N., Bennouna, A., Erraissi, N., Raoufi, M., Asselman, A., et al. (2024). Assessment the long-term performance ratio maps of three grid-connected photovoltaic systems in the Moroccan climate. Energy for Sustainable Development, 79: 101388. https://doi.org/10.1016/j.esd.2024.101388

[11] Haffaf, A., Lakdja, F. (2024). Comprehensive multi-stage 3E feasibility and overall sensitivity analysis of PV-Diesel-BESS hybrid on/off grid system under various battery technologies, energy controls strategies, and solar tracking techniques. Energy Conversion and Management, 312: 118548. https://doi.org/10.1016/j.enconman.2024.118548

[12] Motahhir, S., El Hammoumi, A., El Ghzizal, A. (2020). The most used MPPT algorithms: Review and the suitable low-cost embedded board for each algorithm. Journal of Cleaner Production, 246: 118983. https://doi.org/10.1016/j.jclepro.2019.118983

[13] Yang, B., Xie, R., Duan, J., Wang, J. (2023). State-of-the-art review of MPPT techniques for hybrid PV-TEG systems: Modeling, methodologies, and perspectives. Global Energy Interconnection, 6(5): 567-591. https://doi.org/10.1016/j.gloei.2023.10.005

[14] Tajaldin, K.H., Motlak, H.J. (2024). Enhancement of

DC-DC Luo converter using adaptive PI MPPT and P&O MPPT for photovoltaic system. Journal Européen des Systèmes Automatisés, 57(3): 921-933. https://doi.org/10.18280/jesa.570330

[15] Pan, X., Liang, W., Guo, J., Sun, X., Chen, H. (2024). Parameter Estimation by considering both voltage dip and phase angle jump for DFIG-based WTGs in distribution grids. IEEE Transactions on Sustainable Energy, 15(4): 2170-2181. https://doi.org/10.1109/TSTE.2024.3404400

[16] Zahloul, H., Khaliq, A., Hamzehbahmani, H., Veremieiev, S., Salous, S. (2024). Evaluation of LVRT capability and stability analysis of VSC based advanced control approach for grid connected PV system under grid fault conditions. Heliyon, 10(5): e26935. https://doi.org/10.1016/j.heliyon.2024.e26935

[17] Gawhade, P., Ojha, A. (2022). Grid synchronization techniques: A review. In P. Verma, O.D. Samuel, T.N. Verma, & G. Dwivedi (Eds.), Advancement in Materials, Manufacturing and Energy Engineering, pp. 187-195. Springer. https://doi.org/10.1007/978-981-16-5371-1_17

[18] Kulkarni, S.V., Gaonkar, D.N. (2023). An investigation of PLL synchronization techniques for distributed generation sources in the grid-connected mode of operation. Electric Power Systems Research, 223: 109535. https://doi.org/10.1016/j.epsr.2023.109535

[19] Mondol, J.D., Yohanis, Y.G., Norton, B. (2009). Optimising the economic viability of grid-connected photovoltaic systems. Applied Energy, 86(7): 985-999. https://doi.org/10.1016/j.apenergy.2008.10.001

[20] Gao, F., Shi, Z., Kaiwen Yang, Y.P., Gao, Z., Xu, H., Qiang, Y. (2024). Improved dual-vector model predictive control for common-mode voltage constant on a grid-connected inverter. Journal of Applied Science and Engineering, 28(2): 295-304. https://doi.org/10.6180/jase.202502_28(2).0009

[21] Rehan, M.A. (2024). Optimization of grid-connected hybrid renewable energy system for the educational institutes in Pakistan. e-Prime - Advances in Electrical Engineering, Electronics and Energy, 10: 100781. https://doi.org/10.1016/j.prime.2024.100781

[22] Dunna, V.K., Chandra, K.P.B., Rout, P.K., Sahu, B.K., Manoharan, P., Alsoud, A.R., Derebew, B. (2024). Super-twisting MPPT control for grid-connected PV/battery system using higher order sliding mode observer. Scientific Reports, 14(1): 16597. https://doi.org/10.1038/s41598-024-67083-w

[23] Dey, D., Subudhi, B. (2020). Design, simulation and economic evaluation of 90 kW grid connected Photovoltaic system. Energy Reports, 6: 1778-1787. https://doi.org/10.1016/j.egyr.2020.04.027

[24] Lımem, F., Sezen, S. (2021). Comparative analysis of different photovoltaic simulation software: Case study on analyzing the performance of a 5,1 kWp grid connected photovoltaic system. Avrupa Bilim ve Teknoloji Dergisi, 32: 816-826. https://doi.org/10.31590/ejosat.1040126

[25] Priyadarshi, N., Sharma, A.K., Priyam, S. (2018). An experimental realization of grid-connected PV system with MPPT using dSPACE DS 1104 control board. In Advances in Smart Grid and Renewable Energy, pp. 125-133. https://doi.org/10.1007/978-981-10-4286-7_13

[26] Seo, H.R., Kim, G.H., Ali, M.H., Park, M., Yu, I. (2007). A study on the performance analysis of the grid-connected PV AF system. In 2007 International Conference on Electrical Machines and Systems (ICEMS), pp. 371-375. https://doi.org/10.1109/ICEMS12746.2007.4412259

[27] Zhou, H., Tong, C., Mao, M., Gao, C. (2010). Development of single-phase photovoltaic grid-connected inverter based on DSP control. The 2nd International Symposium on Power Electronics for Distributed Generation Systems, pp. 650-653. https://doi.org/10.1109/PEDG.2010.5545766

[28] Lima, J. C., Corleta, J.M., Medeiros, A., Canalli, V.M., Antunes, F., Libano, F.B., Dos Reis, F.S. (2000). A PIC controller for grid connected PV system using a FPGA based inverter. ISIE'2000. Proceedings of the 2000 IEEE International Symposium on Industrial Electronics (Cat. No.00TH8543), pp. 169-173. https://doi.org/10.1109/ISIE.2000.930506

[29] Xu, X., Chen, J., Li, S., Hu, K., Yu, L. (2011). FPGA implementation of CPS-SPWM for grid connected photovoltaic system. In 2011 Asia-Pacific Power and Energy Engineering Conference, pp. 1-4. https://doi.org/10.1109/APPEEC.2011.5748720

[30] Jaoide, E., Aamri, F. E., Outazkrit, M., Radouane, A., Mouhsen, A. (2024). Maximum power point tracking and space vector modulation control of quasi-z-source inverter for grid-connected photovoltaic systems. International Journal of Electrical and Computer Engineering (IJECE), 14(2): 1424-1436. https://doi.org/10.11591/ijece.v14i2.pp1424-1436

[31] Kar, M.K., Kanungo, S., Dash, S., Parida, R.N.R. (2024). Grid connected solar panel with battery energy storage system. International Journal of Applied Power Engineering (IJAPE), 13(1): 223-233. https://doi.org/10.11591/ijape.v13.i1.pp223-233

[32] Amor, Y.A., Kheldoun, A., Metidji, B., Hamoudi, F., Merazka, A., Lazoueche, Y. (2021). Design and implementation of three-level T-type inverter based on simplified SVPWM using cost-effective STM32F4 board. International Journal of Digital Signals and Smart Systems, 5(1): 20-39. https://doi.org/10.1504/IJDSSS.2021.112792

[33] Mostafa, S., Zekry, A., Youssef, A., Anis, W.R. (2022). Raspberry Pi design and hardware implementation of fuzzy-PI controller for three-phase grid-connected inverter. Energies, 15(3): 843. https://doi.org/10.3390/en15030843

[34] Pillai, S., Thale, S. (2016). Design and implementation of a three phase inverter for renewable energy source with unified control strategy. Energy Procedia, 90: 673-680. https://doi.org/10.1016/j.egypro.2016.11.236

[35] Mejdar, R.S., Salimi, M., Zakipour, A. (2016). Design and implementation of a low cost grid-connected 5 kVA photovoltaic system with load compensation capability. Journal of Power Electronics, 16(6): 2306-2314. https://doi.org/10.6113/JPE.2016.16.6.2306

[36] Boutaghane, K., Bennecib, N., Benidir, M., Benbouhenni, H., Colak, I. (2024). Performance enhancement of a three-phase grid-connected PV inverter system using fractional-order integral sliding mode controls. Energy Reports, 11: 3976-3994. https://doi.org/10.1016/j.egyr.2024.03.049

[37] Debdouche, N., Zarour, L., Benbouhenni, H., Mehazzem, F., Deffaf, B. (2023). Robust integral backstepping

control microgrid connected photovoltaic system with battery energy storage through multi-functional voltage source inverter using direct power control SVM strategies. Energy Reports, 10: 565-580. https://doi.org/10.1016/j.egyr.2023.07.012
[38] Mohammed, A.Y., Mohammed, F.I., Ibrahim, M.Y. (2017). Grid connected photovoltaic system. In 2017 International Conference on Communication, Control, Computing and Electronics Engineering (ICCCCEE), pp. 1-5. https://doi.org/10.1109/ICCCCEE.2017.7867659
[39] Hossain, M.J., Hasan, M.R., Hossain, M., Islam, M.R. (2014). Design and implementation of a grid connected single phase inverter for photovoltaic system. In 2014 3rd International Conference on the Developments in Renewable Energy Technology (ICDRET), pp. 1-6. https://doi.org/10.1109/ICDRET.2014.6861681
[40] Abdelhamid, H., Bahi, T. (2024). Performance analysis of maximum power point tracking for grid-photovoltaic system. Journal Européen des Systèmes Automatisés, 57(3): 689-694. https://doi.org/10.18280/jesa.570306
[41] Satif, A., Hlou, L., Elgouri, R. (2020). A low-cost maximum power point tracking method based on PI controller Arduino implementing. In Advanced Intelligent Systems for Sustainable Development (AI2SD'2019), pp. 12-23. https://doi.org/10.1007/978-3-030-36475-5_2
[42] Satif, A., Hlou, L., Elgouri, R. (2018). An improved perturb and observe maximum power point tracking algorithm for photovoltaic systems. 2018 Renewable Energies, Power Systems & Green Inclusive Economy (REPS-GIE), pp. 1-6. https://doi.org/10.1109/REPSGIE.2018.8488832
[43] Özkan, Z., Hava, A.M. (2014). Three-phase inverter topologies for grid-connected photovoltaic systems. In 2014 International Power Electronics Conference (IPEC-Hiroshima 2014-ECCE ASIA), pp. 498-505. https://doi.org/10.1109/IPEC.2014.6869630
[44] Kumar, K.V., Michael, P.A., John, J.P., Kumar, S.S. (2010). Simulation and comparison of SPWM and SVPWM control for three phase inverter. ARPN Journal of Engineering and Applied Sciences, 5(7): 61-74.
[45] Satif, A., Hlou, L., Zemmouri, A., Dahou, H., Elgouri, R. (2020). Real-time implementation of space vector modulation using Arduino as a low-cost microcontroller for three-phase grid-connected inverter. Indonesian Journal of Electrical Engineering and Informatics (IJEEI), 8(1): 1207. https://doi.org/10.52549/ijeei.v8i1.1207
[46] Guerrero-Rodríguez, N.F., Rey-Boué, A.B., Bueno, E.J., Ortiz, O., Reyes-Archundia, E. (2017). Synchronization algorithms for grid-connected renewable systems: Overview, tests and comparative analysis. Renewable and Sustainable Energy Reviews, 75: 629-643. https://doi.org/10.1016/j.rser.2016.11.038
[47] Kazmierkowski, M.P., Malesani, L. (1998). Current control techniques for three-phase voltage-source PWM converters: A survey. IEEE Transactions on Industrial Electronics, 45(5): 691-703. https://doi.org/10.1109/41.720325
[48] Guerrero-Rodríguez, N.F., Rey-Boué, A.B., Reyes-Archundia, E. (2017). Overview and comparative study of two control strategies used in 3-phase grid-connected inverters for renewable systems. Renewable Energy Focus, 19-20: 75-89. https://doi.org/10.1016/j.ref.2017.05.007
[49] Himabindu, E., Krishna, D., Venkateshwarlu, S., Reddy, K.C. (2024). Fuzzy logic sliding mode controller based UPQC using DC link voltage fed by solar PV to enhance dynamic performance in the power grid. Journal of Applied Science and Engineering, 28(5): 969-978. https://doi.org/10.6180/jase.202505_28(5).0006
[50] Dang, C., Tong, X., Song, W. (2020). Sliding-mode control in dq-frame for a three-phase grid-connected inverter with LCL-filter. Journal of the Franklin Institute, 357(15): 10159-10174. https://doi.org/10.1016/j.jfranklin.2019.12.022
[51] Abubakar, I., Khalid, S.N., Mustafa, M.W., Shareef, H., Mustapha, M. (2017). Calibration of ZMPT101B voltage sensor module using polynomial regression for accurate load monitoring. ARPN Journal of Engineering and Applied Sciences, 12(4): 1076-1084.
[52] Sevilmiş, F., Karaca, H. (2022). Performance enhancement of DSOGI-PLL with a simple approach in grid-connected applications. Energy Reports, 8: 9-18. https://doi.org/10.1016/j.egyr.2021.11.186
[53] Magdy, G., Shabib, G., Elbaset, A.A., Kerdphol, T., Qudaih, Y., Bevrani, H., Mitani, Y. (2019). Tustin's technique based digital decentralized load frequency control in a realistic multi power system considering wind farms and communications delays. Ain Shams Engineering Journal, 10(2): 327-341. https://doi.org/10.1016/j.asej.2019.01.004